Integrated systems biology and imaging of the smallest free-living eukaryote *Ostreococcus tauri*

Authors: Chuck R. Smallwood[1], Jian-Hua Chen[2], Neeraj Kumar[1], William Chrisler[1], Samuel O. Purvine[1], Jennifer E. Kyle[1], Carrie D. Nicora[1], Rosanne Boudreau[2], Axel Ekman[2], Kim K. Hixson[1], Ronald J. Moore[1], Gerry McDermott[2], William R. Cannon[1] & James E. Evans[1,3*]

Affiliations:

1) Earth and Biological Sciences, Pacific Northwest National Laboratory, 902 Battelle Blvd., Richland, WA 99354, USA
2) Department of Anatomy, School of Medicine, UCSF, San Francisco, CA 94110, USA; Molecular Biophysics and Integrated Bioimaging, Lawrence Berkeley National Laboratory, Berkeley, CA 94720, USA
3) School of Biological Sciences, Washington State University, Pullman, WA 99164, USA.

Corresponding Author: james.evans@pnnl.gov

Abstract:

Ostreococcus tauri is an ancient phototrophic microalgae that possesses favorable genetic and cellular characteristics for reductionist studies probing biosystem design and dynamics. Here multimodal bioimaging and multi-omics techniques were combined to interrogate *O. tauri* cellular changes in response to variations in bioavailable nitrogen and carbon ratios. Confocal microscopy, stimulated Raman scattering, and cryo-soft x-ray tomography revealed whole cell ultrastructural dynamics and composition while proteomic and lipidomic profiling captured changes at the molecular and macromolecular scale.

Despite several energy dense long-chain triacylglycerol lipids showing more than 40-fold higher abundance under N deprivation, only a few proteins directly associated with lipid biogenesis showed significant expression changes. However, the entire pathway for starch granule biosynthesis was highly upregulated suggesting much of the cellular energy is preferentially directed towards starch over lipid accumulation. Additionally, three of the five most downregulated and five of the ten most upregulated proteins during severe nitrogen depletion were unnamed protein products that warrant additional biochemical analysis and functional annotation to control carbon transformation dynamics in this smallest eukaryote.

Keywords:

systems biology, proteomics, lipidomics, biofuel, microalgae, photosynthesis, oleaginous, triacylglycerol, lipid, starch, carbon transformation, lipid droplet, nitrogen scavenging, soft x-ray tomography, stimulated raman scattering microscopy, fluorescence microscopy

Introduction

Microalgae are ubiquitous in oceans and maintain a major carbon sink in the complex world-wide ecosystem. Spanning more than one-billion years of evolution, microalgae are

26 phylogenetically diverse and exhibit varying cellular phenotypes that naturally produce high
27 value metabolites, proteins, carbohydrates and energy dense lipids that can be exploited for a
28 wide array of industrial applications [1-3]. Due to their high photosynthetic efficiency for energy
29 conversion, and minimal growth requirements consisting of sustainable resources such as
30 marine or brackish media, light, CO_2 and trace vitamins, microalgae are prime bioproduction
31 platforms [4,5].

32 Triacylglycerol (TAG) lipids are significantly enhanced when microalgae are subjected to
33 cellular stressors such as light, temperature, and nutrient deprivation [6]. TAG lipids possess
34 nonpolar character and are stored in anhydrous, high-density organelles called lipid bodies,
35 which are desirable for industrial lipid feedstock applications [7]. For other oleaginous algae, TAG
36 production can be triggered by nutrient deprivation of iron, sulfur, nitrogen, phosphate, or silicon
37 [6]. In most eukaryotes, combinatorial reduction of these nutrients results in altered levels of
38 growth-associated structural lipids (phospholipids) and energy storage lipids (TAG) products [8,9].
39 Unfortunately, in most cases starvation or deprivation can be detrimental to cell viability and
40 overall growth capacity thereby limiting cell biomass yields needed for viable lipid feedstock
41 industrial applications [10]. While several reports have shown that supplementing additional C
42 sources when combined with N depletion for certain organisms can yield increased growth and
43 lipid accumulation rates compared to strict starvation[2,11,12,13], a detailed understanding of the
44 interplay between carbon and nitrogen bioavailability is needed to advance bioproduction
45 applications.

46 Studying phototrophic metabolism in primitive species, such as the prasinophyte
47 *Ostreococcus tauri* can provide convenient opportunities to define minimal and critical metabolic
48 pathways for C transformation[14,15,16]. *O. tauri* is the smallest known free-living eukaryote
49 (~0.8μm in thickness), lacks a cell wall, and thrives in varying photic, toxic and thermal
50 ecosystems[17-19]. It also has a highly condensed genome with only ~8,000 genes[20] so most

51 reactions are governed by a single enzyme (rather than multiple duplicating function enzymes)
52 which simplifies engineering requirements and interpretation. For example, the canonical model
53 green alga *Chlamydomonas* has 4 copies of Acetyl-CoA Carboxylase (E.C. 6.4.1.2) whereas
54 *Ostreococcus* has only 1 enzyme of that class. In addition, a recent study[21] reported the genetic
55 diversity associated with large phenotypic differences between *Ostreococcus* strains
56 highlighting the uncharted abundance of genetic biodiversity. These characteristics make *O.*
57 *tauri* a potential candidate for future industrial applications. However, considerable biodesign
58 efforts will likely be needed to develop an efficient cell factory for controlled and cost-effective
59 bioproduction of lipid feedstocks or other high value metabolites. Here, an integrated analysis
60 of bioimaging, proteomic, and lipidomic characterization was used to investigate *O. tauri* cellular
61 response to varying C:N ratios. Our results provide additional understanding of C storage and
62 energy transformation pathways within the microalgae *O. tauri* and identify new proteins to
63 target for future engineering efforts.
64
65 **Results**
66 Other than the bioavailable C:N ratio, all other experimental parameters (e.g.,
67 temperature, duration, diurnal cycling, light fluence, etc.) were kept constant throughout this
68 study. The four different media conditions used herein are designated as K6CN, K2CN, K2C
69 and K6C which are listed in decreasing C:N ratio. The normal growth media for *O. tauri* is Keller
70 Media (referenced herein as K2CN media) and contains ~2.5mM bicarbonate and 0.9mM total
71 nitrogen. To streamline interpretation, bicarbonate was kept as the sole media carbon source.
72 For K6CN media the nitrogen content was kept equivalent, but the bicarbonate increased to
73 6mM providing elevated carbon but normal nitrogen conditions. The use of 6mM bicarbonate as
74 the elevated carbon set point was chosen following an initial growth screen of *O. tauri* in K
75 media supplemented with various levels of bicarbonate from 0-10mM where 6mM showed

76 highest growth response with healthy chlorophyll ratios per cell. The final two media conditions
77 K2C and K6C share the same composition as K2CN and K6CN but are depleted of all nitrogen
78 sources. Thus all subsequent experiments consisted of 4 conditions of decreasing C:N
79 bioavailable ratios from elevated carbon with normal nitrogen (K6CN), to normal carbon with
80 normal nitrogen (K2CN), to normal carbon with no nitrogen (K2C), and elevated carbon with no
81 nitrogen (K6C).

82 Diurnal cycling with 12:12 hour light:dark cycles was used to synchronize cellular
83 division and growth, and samples were harvested 3 hours after light to dark transition. Cell
84 growth was monitored by absorbance at 750nm (measure of particulates) and 680nm (measure
85 of chlorophyll a) for up to 144 hours (Fig. 1B). Decreases in absorbance at 680nm were typical
86 of K2C and K6C cell cultures relative to K2CN and K6CN. Absorbance at 750nm exhibited
87 similar decreases for N deprived cultures versus N replete. However, when comparing normal C
88 to excess C for either N replete or N deprived conditions, cultures with excess C consistently
89 displayed higher A680 and A750 values. Confocal fluorescence microscopy was used to
90 compare phenotypes for a couple dozen cells from each condition whereas fluorescence
91 activated cell sorting (FACS) allowed quantitative analysis of larger population dynamics every
92 24 hours. In both case, dramatic increases of neutral lipid (NL) content were detected for K2C
93 and K6C conditions (Fig. 1 C–F). Interestingly K6CN (Fig. 1C) cell cultures only exhibited subtle
94 differences between NL and some increases in phospholipid (PL) intensity indicating some
95 photosynthetic lipid metabolism difference to K2CN (Fig. 1D). Since confocal microscopy can
96 only track dynamics for fluorescently labelled components, label-free cell ultrastructure and
97 composition changes were also evaluated.

98 Cryogenic soft x-ray nanotomography (CSXT) was performed on 72-hour cell cultures to
99 increase resolution and highlight native cellular features of intracellular lipid accumulation (Fig.
100 1E). Dark subcellular features, assigned as vacuoles due to their linear absorption coefficient

101 (LAC), were observed in the intracellular cytosolic space of cells in K6CN and K2CN culture
102 conditions, but no vacuoles were observed for K2C and K6C cultured cells. The vacuoles were
103 much larger in K6CN compared to K2CN conditions. Based on studies conducted in other algae
104 and plants starch is likely present in the chloroplast[20]. However, intracellular starch was
105 undetected in *O. tauri* cells via X-ray nanotomography likely due to the density appearing similar
106 to or masked by the surrounding tissues with a similar LAC - possibly due to its small cell size or
107 chloroplast packing density. Therefore, stimulated Raman scattering (SRS) microscopy was
108 used as a second label-free imaging method to identify relative abundance of intracellular starch
109 accumulation. Interestingly, starch was detected in the chloroplast for all tested conditions.
110 However, the starch seen for K2C was minimal (Supplemental Figure 1). Considering that K6C
111 represents an even more deprived nitrogen to carbon ratio compared to K2C, it was anticipated
112 that K6C would show the lowest levels of starch since both conditions also show significant lipid
113 accumulation. However, the increase in starch content for K6C suggests that these cells still
114 have abundant carbon available for transformation into carbohydrates, and potential future
115 engineering efforts could focus on knocking out genes associated with starch accumulation to
116 divert this excess energy toward lipid feedstock production instead.
117 The confocal imaging also happened to capture a possible lipid droplet secretion event.
118 During live-cell imaging, a single cell was captured over a few minutes showing the formation of
119 a cellular bleb containing a single lipid droplet that was released in subsequent scans
120 (Supplemental Figure 2). We have previously reported that this organism does not appear to
121 have any canonical proteins associated with lipid droplet secretion from other organisms[22]. That
122 study also captured static images showing what was described as blebbing intermediates. The
123 current image series reported here is the first case in which the process was observed live
124 thereby lending additional support to the theory that *O. tauri* is capable of lipid droplet secretion
125 although the detailed mechanism remains elusive.

126 Dramatic changes observed for lipid staining profiles prompted the exploration of
127 underlying global proteomic expression profiles for each experimental culture condition.
128 Cultures were harvested at 24- and 48-hour time points for LC-MS/MS proteomics to obtain a
129 measure of global proteomic expression. These time-points were chosen for comparison since
130 they showed the biggest relative 24-hour changes via FACS and confocal analysis. The
131 proteomics data was mapped into individual metabolic groups (synthesis, degradation, energy,
132 other and non-metabolic pathways) to interpret relative changes of cells cultured in K6CN,
133 K2CN, K2C and K6C conditions for each metabolic pathway (Fig. 2). Of particular note was the
134 increased changes in abundance for both K2C and K6C in the carbohydrate synthesis pathway
135 compared to K2CN and K6CN. However, very few proteins within the fatty acid (FA)/lipid
136 synthesis pathways showed significant, if any, change in abundance despite bioimaging
137 observations of cellular lipid increases up to 60% the volume of cells. For example, while DGAT,
138 the canonical enzyme representing the last committed step of TAG synthesis was detected with
139 global proteomics, it's abundance remained effectively equivalent across all 4 sample
140 conditions.
141 High C to N ratio of K6C displayed consistently higher proteomic responses compared to
142 K2C for upregulated proteins related to C storage. The complete starch pathway was detected
143 with ascending upregulation from alpha amylase to granule-bound starch synthetase (GBSSI)
144 for N depletion conditions. GBSSI was the third highest upregulated protein overall highlighting
145 the reliance on carbon storage under these conditions. Previous studies have found similar
146 results for GBSSI[23]. N deprivation also caused downregulation of proteins involved in N
147 acquisition, such as nitrate transporters, nitrate reductase with concomitant upregulation of N
148 scavenging proteins for glutamine, asparagine, and urea. Much of the downregulated proteins
149 detected were ribosome based or were proteins localized to the chloroplast.

150 Overall 471 unnamed protein products were found to be upregulated or downregulated
151 with several exhibiting some of the most extreme abundance changes (Fig. 4). N deplete
152 conditions K2C and K6C had similar distributions of upregulated and downregulated protein
153 trends, with more increased upregulation of proteins for excess carbon cultures. For K6C, 5 of
154 the 10 most upregulated and 3 of the 10 most downregulated were UPP (Fig. 3). Interestingly,
155 several of these proteins show inversion of abundance for replete versus depleted N conditions.
156 XP_003075209 (ostta02g03680), XP_003081059 (ostta09g00670), XP_003078347
157 (ostta03g04500) all exhibit significant upregulation under K6CN and K2CN conditions at 48
158 hours compared to K2CN at 24 hours, however, these proteins show significant downregulation
159 for K2C and K6C conditions at 48 hours. The biggest change was seen for XP_003078347
160 (ostta03g04500) which was had a log2 value change of -0.54 for K6CN but a value of 1.96 for
161 K6C. Similarly, other unnamed proteins XP_003084215 (ostta18g01710), XP_003082140
162 (ostta11g03180) and XP_003082699 (ostta13g02170) were all downregulated for K6CN and
163 K2CN at 48 hours but upregulated for K2C and K6C. Clearly these unnamed proteins are
164 dramatically affected by the bioavailable ratio of C and N and represent interesting targets for
165 future in-depth functional annotation.
166 Conducting a BLAST alignment analysis on the UPP identified in these runs resolved a
167 predicted membrane protein (XP_003080099 (ostta06g04530)) upregulated for N depleted
168 conditions K2C and K6C, which was identified as having a domain with homology to TMEM14,
169 an uncharacterized superfamily believed to be involved in membrane transport of lipids in higher
170 eukaryotes. This protein could possibly play a role in the lipid droplet secretion from *O. tauri*.
171 Other potentially interesting unknown protein products were also uncovered during BLAST
172 alignments with two notable probable identifications: A putative Acyl-CoA N-acyltransferase
173 (XP_003084085.1 (ostta18g00460)) slightly upregulated for K2CN and K2C but not K6CN or
174 K6C; and a putative Zinc finger (XP_003080741.1 (ostta08g01730)) slightly downregulated for

175 K6CN, K6C, and K2C conditions, which have been known to participate in a number of
176 eukaryotic cellular mechanisms including lipid binding. Additional proteins such as sarcosine-
177 dimethyltransferase (SDMT), an enzyme found in the betaine biosynthesis pathway in other
178 algae and higher plants related to osmoprotection during cellular stress[24,25], were found to be
179 elevated only for K2C and K6C conditions, which may reinforce cellular stability during N stress
180 and lipid accumulation.

181 Despite observing limited changes in the proteome related to lipid metabolism, the visual
182 confocal and FACS analysis provided ample evidence of significant lipid accumulation that
183 warranted further characterization to understand cellular lipid composition and relative
184 abundance. Thus, the same K6CN, K2CN, K2C, and K6C cultures were surveyed at the same
185 24- and 48-hour time-points using LC-MS/MS global lipidomics analysis. Quantitative lipid
186 profiles were collected for more than 280 lipids (Supplemental Figures 3 – 9). The N depletion
187 conditions (K2C and K6C) resulted in significant increases of energy dense TAG lipids with
188 more than 10 TAGs showing >40-fold increase in abundance already at 48-hours. The FACS
189 and confocal analysis showed that the NL content continues to accumulate well beyond 48
190 hours. In comparison, TAG lipid abundance was flat or decreased for K6CN and K2CN
191 conditioned cells, indicating that cells were not diverting C into lipid energy storage during
192 nutrient rich conditions although they were still accumulating starch as seen from SRS
193 (Supplemental Figure 1). The observed FA profiles provide additional support for recently
194 reported[26] unique long chain FAs despite lacking annotated enzymes known to synthesize
195 them, indicating that *O. tauri* is at the very least an intriguing oleaginous organism for lipid
196 feedstock development. In addition, the number of long chain FAs in TAGs were significantly
197 enhanced during K6C conditions, demonstrating this organism's capacity to uptake and
198 transform excess C into long chain energy dense lipids without genetic modification
199 (Supplemental Figures 7–9).

200 Changes in structural lipids were also detected (Supplemental Figures 3 – 6).
201 Thylakoidal membranes are composed of monogalactosyldiacylglycerol (MGDG) and
202 digalactosyldiacylglycerol (DGDG), which stabilize the thylakoid for maximal photosynthetic
203 efficiency [27]. In addition, algal thylakoid membranes contain abundant amounts of
204 sulphoquinovosyldiacylglycerol (SQDG) which contributes to increased stability in the
205 photosynthetic harvesting complexes and accommodates membrane protein associations
206 unique to microalgae [28]. Increased abundances for MGDG and 3- to 7-fold increases in DGDG
207 were detected for K2C and K6C conditions, with C16 chain lengths exhibiting the most
208 abundant and dramatic changes during N depletion. C16 chain length SQDG lipids were also
209 slightly upregulated for K6C, suggesting they may be adding stability to light harvesting
210 complexes or membrane protein expression unique to excess C exposure and N depletion.
211
212 **Discussion**
213 Linkages between N and C metabolism related to lipid biogenesis were interrogated for
214 the microalgae *Ostreococcus tauri*. Single cell and population imaging experiments combined
215 with global proteomic and lipidomic experiments on the same cultures demonstrated that even
216 the simplified cell architecture and genome of *O. tauri* displays complicated regulatory linkages
217 as a function of bioavailable carbon to nitrogen ratios. Cryogenic soft x-ray nanotomography
218 revealed distinct lipid droplet distributions of varying sizes confirming initial fluorescence
219 microscopy results. K2C conditioned cells had uniform sized lipid droplets whereas cells in K6C
220 conditions had lipid droplets of varying size including very large lipid droplets that swelled and
221 deformed the cells.
222 Numerous photosynthetic, structural, and energy storage fatty acid (FA)/lipids were
223 verified through LC–MS/MS lipidomic analysis that included detection of long chain TAGs, ideal
224 for lipid feedstocks. Proteomic data combined with physiological cell responses to varying C and

225 N revealed that although FA/lipid synthesis pathways had little proteomic changes,
226 carbohydrate synthesis proteomics was independently upregulated. Both ribulose 1,5-
227 biphosphate carboxylase/oxygenase large and small subunits (Rubisco) were slightly
228 downregulated for K2C and K6C relative to K2CN suggesting Rubisco expression in
229 *Ostreococcus* contains minimum concentrations of Rubisco to support normal growth as
230 reported for other organisms[29]. Restricting protein identifications to subsets related to
231 carbohydrate conversion, N scavenging, and energy regulation allowed for the simplification of
232 biological interpretations related to lipid feedstock optimization targets. The most upregulated
233 protein was a protein kinase involved in serine/threonine phosphorylation and was equally
234 upregulated for K2C, K6C, and K6CN conditions, which could possibly play a role in regulating
235 diurnal cycling or stress response since K6CN could also be seen as another N deprived state
236 relative to available C. GBSSI was the third most upregulated protein in all and was more
237 upregulated in K6C than K2C. Knock-down of GBSSI could potentially provide a redirection of
238 *O. tauri* metabolism to less starch accumulation and more lipid accumulation under K6C
239 conditions.
240 In addition to the proteins related to energy storage, increased abundances of proteins
241 related to lipid viability, lipid production, and osmotic shock were detected to varying degrees.
242 Finally, a surprising number of proteins of unknown function and identity were revealed to be
243 part of the 10 most significant proteomic increases and decreases overall and each is a
244 potential target for future engineering efforts. A recent study focused on circadian protein
245 regulation[30] identified ostta03g04500, ostta09g00670, and ostta02g03680 proteins of unknown
246 function that happen to overlap with the findings reported here. This suggests that the proteins
247 found in both studies may have a co-relational effect between carbon and nitrogen
248 bioavailability and the circadian cycle. Delving further into the function of these individual
249 proteins will be important for understanding their real role in overall cellular regulation and

250 metabolic processes. Furthermore, the wealth of undefined proteins emphasizes the extent of
251 unexplored opportunities related to N, C, and energy storage pathways, and highlights the
252 peculiar genetic diversity within natural populations of *Ostreococcus* and possibly other primitive
253 marine species.
254
255 **Methods:**
256 **<u>Strain maintenance, culture growth media, and nutrient starvation conditions</u>**
257 *O. tauri* cell cultures were obtained from the Roscoff Culture Collection (RCC745); strain name:
258 OTTH0595, which has been fully sequenced [20]. Cultures of RCC745 were grown in defined
259 Keller (K) media[31] with normal or depleted N and HCO_{3-}: K2CN contained normal N and C,
260 K6CN with normal N and 6mM HCO_{3-}, K2C with depleted N and 2.5mM HCO_{3-}, and K6C with
261 depleted N and 6mM HCO_{3-}. All Keller media-based culture conditions were prepared in fresh
262 artificial seawater (ASW) with defined amounts of nutrients analytically prepared fresh and
263 sterile filtered prior to each experiment. To monitor growth and lipid accumulation over time
264 absorbance at 680nm and 750nm was measured to obtain both values for chlorophyll content
265 and particulate matter, respectively, for each culture. Graphing the ratio of 750nm/680nm
266 provided a measure of chlorophyll functional efficiency as well as possible lipid particulates in
267 solution. Graphical analysis of each growth and starvation curve required minimal normalization
268 due to our consistent efforts in capturing cells during mid-log stages of growth. For growth and
269 lipid accumulation studies cells were grown initially in normal K media to approximately 0.03 at
270 OD680 then gently centrifuging cultures at 1200XG for 10 minutes in a swing bucket rotor,
271 washed with respective defined K media, and resuspending cells into defined K media at a
272 target 0.03 at OD680 and continued diurnal light entrainment for specified time courses in
273 sealable CytoOne non-treated cell culture flasks (USA Scientific, USA) with mixing of cultures
274 once per 24 hours. To prepare cell cultures for starvation surveys they were gently centrifuged

275 fresh cultures at 2200xG for 10 mins with swing bucket rotor centrifugation and washed cell
276 pellets once with defined K media of interest then suspended cells in defined media conditions
277 and continued diurnal light entrainment for specified time courses in sealable CytoOne non-
278 treated cell culture flasks (USA Scientific, USA) with mixing of cultures once per 24 hours.
279

280 **Fluorescence activated cell sorting analysis of intracellular lipid content**

281 *O. tauri* cells were cultured to mid log phase and gently centrifuged to concentration then
282 stained with Nile Red (4.8μg/mL) lipid stain for exactly 10 mins before each experimental
283 measurement on the BD INFLUX flow cytometer (BD Biosciences, San Jose, CA, USA). FSC
284 and SSC were used to gate out any non-specific cellular debris. Specific gating in the range of
285 known cell size of *O. tauri* was used to determine the fluorescence from stained neutral lipid
286 (488/542±13.5 nm), phospholipid (561/615±12 nm), and natural chlorophyll autofluorescence
287 (640/670±15 nm) for defined populations of cells. Each individual FACS experiment was
288 calibrated to 3.6 ide scatter 10 mins before running our sample measurements in defined media
289 cultures. The fluorescence intensity of neutral lipid and phospholipid fluorescence intensity at
290 specific time points was compared in scatter plots to demonstrate population dynamics for each
291 sample condition. K2CN at 24 hours was used as the baseline for normal conditions to detect
292 changes due to varying C:N bioavailability.
293

294 **Fluorescence and SRS confocal microscopy**

295 Confocal images were obtained on Zeiss LSM 710 (Carl Zeiss AG, Germany) confocal
296 microscope with a 100x oil immersion objective. An InTune Laser with 505nm and 535nm light
297 was used to maximize the separation of the triglyceride (585nm) and phospholipid (638nm)
298 emission peaks while diminishing crosstalk of the Nile Red stained cells. In addition, chlorophyll
299 autofluorescence was excited with 405nm light and monitored the emission profile at 680nm.

300 Nile Red stained cells were immobilized on glass slides with poly-L-lysine and imaged
301 immediately with z-scan slicing of 0.43μm to survey whole cell fluorescence labeling distribution.
302 All fluorescence channels were set with identical gain and laser power settings to provide
303 relative levels of fluorescent intensity and no adjustments of contrast or gain were applied to
304 fluorescence imaging during post processing. *O. tauri* cultures were grown in 15mL falcon tubes
305 in a 12:12 light:dark illumination (~20 μmol/m^2/s) at 25ºC for 96 hours, harvested by gentle
306 centrifugation (1000xG, 5 mins) and concentrated equally to 10x original cell density for
307 imaging. Concentrated cell suspensions were then stained with Nile Red (4.8 μg/mL) for 10
308 minutes and then 3μL of the labeled culture were mounted on poly-lysine treated microscope
309 slides (Electron Microscopy Sciences, USA) for confocal fluorescence and SRS imaging.
310 Fluorescence and SRS confocal microscopy were conducted on the Nile Red stained *O. tauri*
311 cells using a Leica DMi8 (Leica Microsystems GmbH, Germany) inverted confocal microscope
312 (a 63x/1.20na water immersion objective) integrated with an APE picoEmerald laser consisting
313 of a 2.5 ps pulsed tunable pump and 1031nm stokes with the SRS detection module and an
314 EOM Modulator. Prior to the SRS detection, the stokes beam was blocked by a FESH1000 filter
315 (Thorlabs, USA). The SRS signal was detected on a 10x10mm photodiode connected to the
316 APE lock-in amplifier. For starch detection the SRS pump signal was tuned to 947nm at 152mW
317 with bandwidth of 0.7nm with the stokes power at 150mW modulated by the integrated EOM,
318 and a delay of 3500fs to detect the 860cm^{-1} peak of starch [32]. Cellular chlorophyll was excited
319 with a 638nm laser with 1% power and fluorescence signal collected with emission range of
320 677–689nm. Neutral lipid fluorescence from Nile Red staining was excited with 552nm with 1%
321 laser power and emission 575–583nm. Sequential acquisition of different channels was
322 acquired at 1024x1024 format, with slower 400 scan speeds, and 4x zoom. Maximum
323 thresholds were changed consistently for all SRS starch images to obtain equal post processing
324 values across all samples; no post processing was conducted on either chlorophyll or neutral

325 lipid channels.

326

327 **Cryogenic Soft X-ray Tomography for Intracellular Distribution of Organelles**

328 Cell cultures were grown on-site at the Advanced Light Source (ALS) at Lawrence
329 Berkeley National Laboratory with a homemade 470nm light source with a measured intensity of
330 20μE. Cell cultures were incubated with 12-hour diurnal light at RT and harvested by
331 centrifugation at 48, 72 and 96-hour time points. Cells were gently centrifuged at 1000xG for
332 10mins to pellet. Pelleted cells had all but ~5μL of supernatant removed to remove a viscous
333 cell biomass. Wet cell biomass was inserted into 5μm micro capillaries and plunge frozen in cold
334 liquid propane. In some cases, 6μm polystyrene beads were added to cell suspensions prior to
335 centrifugation to minimize the impact of freezing on large lipid containing cells. Frozen
336 capillaries were stored in liquid nitrogen until imaging by the soft x-ray light source. Soft x-ray
337 data acquisition was carried out on beamline 2.1, a soft x-ray microscope in the National Center
338 for X-Ray Tomography (NCXT) located at the Advanced Light Source in Berkeley, California[33].
339 The microscope soft x-ray illumination was generated by a bend-magnet in the synchrotron
340 lattice and focused onto the specimen by a Fresnel Zone Plate (FZP) condenser. Specimen
341 illumination was order-sorted by a pinhole positioned just in front of the specimen. A second
342 zone plate, located downstream of the specimen, magnified and focused an image of the
343 specimen on a CCD detector. During data collection, the cells were maintained in a stream of
344 helium gas that had been cooled to liquid nitrogen temperatures. Each tomographic dataset
345 (i.e., 90 projection images spanning a range of 180°) was collected using Fresnel zone plate
346 based objective lens with a resolution of 50 nm. Exposure times for each projection image
347 ranged from 150 to 300 msec. The software suite AREC3D was used to align the projection
348 images calculate tomographic reconstructions[34].

349

350 **Lipid Extraction and Lipidomics Using Liquid Chromatography Tandem Mass**
351 **Spectrometry**

352 Each *O. tauri* culture was harvested at specific time points and ultimately spun down at
353 3000 x g for 10 min to form a pellet in chloroform compatible 2 mL Safe Seal microfuge tubes
354 (Sorenson Bioscience, Inc, Salt Lake City, UT). The supernatant was removed, and the wet
355 pellet was weighed for an estimate of biomass, then a mixture of 1 mL of methanol, 0.5 mL of
356 chloroform and 0.4 mL of nanopure water was added to each pellet. The pellets were vortexed
357 and sonicated for about 10 sec in a bath sonicator and the mixture was allowed to stand at room
358 temperature for 10 min. Then an additional 0.5 mL of chloroform and 0.5 mL of water were
359 added, and the mixtures were shaken vigorously into an emulsion. Each sample was
360 centrifuged at 10,000 x g for 10 min. The bottom chloroform layer was carefully removed from
361 the separated solvent layers using a Pasteur pipette and taking care not to take up any of the
362 protein disc or the top polar layer and was placed in a pre-weighed glass auto sampler vial. The
363 bottom lipid layer was dried down overnight under nitrogen and the vials with the total lipid
364 extract (TLEs) were weighed to obtain the total mass. 5μL of chloroform was added to each
365 dried sample and then the sample diluted to 50 μg/μL with methanol. The samples were then
366 stored at –20 °C until ready for mass spectrometric analysis.

367 Extracted lipids were dried down then reconstituted in methanol. The TLEs were
368 analyzed by LC-MS/MS using a Waters NanoAquity UPLC system interfaced with a Velos
369 Orbitrap mass spectrometer (Thermo Scientific, San Jose, CA) as outlined in Dautel et al.
370 2017[35]. LC-MS/MS raw data files were imported into the in-house developed software LIQUID[36]
371 for identification of lipid molecular species. Manual validation of the lipid identifications were
372 determined by examining the tandem mass spectra for diagnostic ion fragments along with
373 associated chain fragment information. In addition, the isotopic profile, extracted ion
374 chromatogram (XIC), and mass error of measured precursor ion were examined for lipid

375

376 **Cellular Protein Extraction and Digestion**

377 To the remaining protein/debris pellet obtained from the lipid extraction, 1 mL of ice cold
378 methanol was added 3 x to wash the majority of residual metabolites away from the pellet. A
379 Filter-Aided Sample Prep (FASP) protein extraction and trypsin digestion was then performed
380 using the FASP protein digestion kit (Expedeon, San Diego CA) using manufacturer's
381 suggested protocol (Erde J et al, 2014, J Proteome Res 13(4):1885-1895). Briefly, methanol
382 washed pellets were air dried for 2 hrs and were resuspended in solubilization buffer of 12 mM
383 deoxycholate, 12 mM N-lauroyl sarcosine with 10 mM TCEP, and 200 mM ammonium
384 bicarbonate, pH 8.0 at an approximate concentration of 13 μg/μL. 30 μL of this protein solution
385 was then mixed with 200 μL of urea sample solution (kit provided), the sample was centrifuged
386 on the kit provided spin filter at 14,000 x g for 15 min. Washes with urea and ammonium
387 bicarbonate along with trypsin digestion and alkylation with iodoacetamide were carried out as
388 the kit specifies. Peptides were then suspended in nanopure water and peptides were then
389 quantified using a BCA assay (Pierce, Rockford IL) with a bovine serum albumin standard.

390

391 **iTRAQ Peptide Labeling**

392 Peptides were labeled with 8-plex iTRAQ (AB Sciex, Redwood City, CA) reagents as
393 described below. 100 μg of each peptide sample was placed in a new tube and dried down.
394 Chanel designations are as follows: 43 μg of dissolution buffer (iTRAQ buffer kit) was added to
395 each sample, these being vortexed into solution and centrifuged briefly to draw sample to the
396 bottom of each tube. The iTRAQ reagent (30 μL) was diluted further with isopropanol (115 μL)
397 and this was then added to each sample. Each reaction was carried out at RT for 2 hrs, with 50
398 mM ammonium bicarbonate (200 μL) added to quench each reaction tube. After 1 hr, the
399 contents from all iTRAQ channel reactions were added to one tube and then the sample was

400 vortexed and dried down in a speed vac. The labeled peptides were cleaned up using C-18
401 SPE columns (SUPELCO Discovery) were then employed to remove the salts, using a 0.1%
402 TFA in nanopure water to wash the peptides and 80% acetonitrile, 0.1% TFA in water to elute
403 the peptides.
404
405 Offline Fractionation of Peptides and Preparation of Proteome Samples
406 400 μg of iTRAQ labeled peptides were separated using an off-line high pH (pH 10) reversed-
407 phase (RP) separation with a Waters XBridge C18 column (250 mm x 4.6 mm column
408 containing 5 μm particles and a 4.6 mm x 20 mm guard column) using an Agilent 1200 HPLC
409 System. The sample loaded onto the C18 column was washed for 15 min with Solvent A (10
410 mM ammonium formate, adjusted to pH 10 with ammonium hydroxide). The LC gradient started
411 with a linear increase of Solvent B (10 mM ammonium formate, pH 10, 90% acetonitrile in
412 water) to: 5% over 10 min, 45% Solvent B over 65 min, and then a linear increase to 100%
413 Solvent B over 15 min. Solvent B was held at 100% for 10 min, and then was changed to 100%
414 Solvent A, this being held for 20 min to recondition the column. The flow rate was 0.5 mL/min.
415 A total of 96 fractions were collected into a 96 well plate throughout the LC gradient. The high
416 pH RP fractions were then combined into 12 fractions using the concatenation strategy
417 previously reported[37]. Peptide fractions were dried down and re-suspended in nanopure water
418 at a concentration of 0.075 μg/ μL for mass spectrometry analysis using a Q Exactive HF Hybrid
419 Quadrupole-Orbitrap MS (Thermo Scientific) system as described below.
420
421 **Mass-Spectrometry Based Analysis of Samples**
422 All peptide samples were analyzed using an automated home-built constant flow nano
423 LC system (Agilent) coupled to an Q Exactive HF Hybrid Quadrupole-Orbitrap MS (Thermo
424 Fisher Scientific). Electrospray emitters were custom made using 150 μm o.d. x 20 μm o.d. x

425 20 μm i.d. chemically etched fused silica. An on-line 4-cm x 360 μm o.d. x 150 μm i.d. fused-
426 silica capillary analytical column (3 μm Jupiter C18) was used. Mobile phases consisted of
427 0.1% formic acid in water (A) and 0.1% formic acid acetonitrile (B) operated at 300 nL/min with
428 a gradient profile as follows (min:%B); 0:5, 2:8, 20:12, 75:35, 97:60, 100:85.
429
430 **Peptide Identification, Quantification and Analysis**
431 For peptide identification, MS/MS spectra were searched against a decoy O. tauri
432 database using the algorithm SEQUEST. An approach to correlate tandem mass spectral data
433 of peptides with amino acid sequences in a protein database[38]. Search parameters included: no
434 enzyme specificity for proteome data and trypsin enzyme specificity with a maximum of two
435 missed cleaves, ± 50 ppm precursor mass tolerance, ± 0.05 Da product mass tolerance, and
436 carbamidomethylation of cysteines and iTRAQ labeling of lysines and peptide N-termini as fixed
437 modifications. Allowed variable modifications were oxidation of methionine. MSGF+ spectra
438 probability values were also calculated for peptides identified from SEQUEST searches[39].
439 Measured mass accuracy and MSGF spectra probability were used to filter identified peptides to
440 <0.4% false discovery rate (FDR) at spectrum level and <1% FDR at the peptide level using the
441 decoy approach. iTRAQ reporter ions were extracted using the MASIC software[40] for fast
442 quantitation and flexible visualization of chromatographic profiles from detected LC-MS(/MS)
443 features with a 10-ppm mass tolerance for each expected iTRAQ reporter ion as determined
444 from each MS/MS spectrum.
445 Relative abundances of peptides were determined using iTRAQ reporter ion intensity
446 ratios from each MS/MS spectrum. Individual peptide intensity values were determined by
447 dividing the base peak intensity by the relative ratio associated with each reporter ion. All
448 peptide values were then transformed into log2 values for comparison between conditions.

Acknowledgements:

This research was performed using the Environmental Molecular Sciences Laboratory (EMSL), a national scientific user facility sponsored by the Department of Energy's Office of Biological and Environmental Research and located at PNNL. This research also used resources of the Advanced Light Source, which is a DOE Office of Science User Facility under contract no. DE-AC02-05CH11231.

Funding

This work was supported by DOE-BER Mesoscale to Molecules Bioimaging Project FWP# 66382.

Competing Interests: We declare no competing interests.

Contributions

JEE devised and managed all experiments with input from CRS. CRS conducted confocal and Raman imaging experiments and coordinated integrated omics analysis. KKH and CDN performed lipid and proteomics sample prep. RM collected proteomics data that SP analyzed, and NK and WRC worked into the cell model. JEK performed lipidomic data collection and lipidomic analysis. Cryogenic soft X-ray sample preparation was conducted by JHC, RB and CRS with JHC and GM acquiring tilt series for subsequent reconstruction by AE. FACS analysis was conducted by WC. JEE and CRS wrote initial manuscript and all authors edited and approved final text.

References

1 Gimpel, J. A., Henriquez, V. & Mayfield, S. P. In Metabolic Engineering of Eukaryotic Microalgae: Potential and Challenges Come with Great Diversity. *Front Microbiol* **6**, 1376, doi:10.3389/fmicb.2015.01376 (2015).
2 Wase, N., Tu, B., Allen, J. W., Black, P. N. & DiRusso, C. C. Identification and Metabolite Profiling of Chemical Activators of Lipid Accumulation in Green Algae. *Plant Physiol* **174**, 2146-2165, doi:10.1104/pp.17.00433 (2017).
3 Longworth, J., Wu, D., Huete-Ortega, M., Wright, P. C. & Vaidyanathan, S. Proteome response of Phaeodactylum tricornutum, during lipid accumulation induced by nitrogen depletion. *Algal Res* **18**, 213-224, doi:10.1016/j.algal.2016.06.015 (2016).
4 Levering, J., Broddrick, J. & Zengler, K. Engineering of oleaginous organisms for lipid production. *Curr Opin Biotechnol* **36**, 32-39, doi:10.1016/j.copbio.2015.08.001 (2015).
5 Liao, J. C., Mi, L., Pontrelli, S. & Luo, S. Fuelling the future: microbial engineering for the production of sustainable biofuels. *Nat Rev Microbiol* **14**, 288-304, doi:10.1038/nrmicro.2016.32 (2016).
6 Goncalves, E. C., Wilkie, A. C., Kirst, M. & Rathinasabapathi, B. Metabolic regulation of triacylglycerol accumulation in the green algae: identification of potential targets for engineering to improve oil yield. *Plant Biotechnol J* **14**, 1649-1660, doi:10.1111/pbi.12523 (2016).
7 Klok, A. J., Martens, D. E., Wijffels, R. H. & Lamers, P. P. Simultaneous growth and neutral lipid accumulation in microalgae. *Bioresour Technol* **134**, 233-243, doi:10.1016/j.biortech.2013.02.006 (2013).
8 Griffiths, M. J., van Hille, R. P. & Harrison, S. T. L. Lipid productivity, settling potential and fatty acid profile of 11 microalgal species grown under nitrogen replete and limited conditions. *J Appl Phycol* **24**, 989-1001 (2012).
9 Guarnieri, M. T., Nag, A., Yang, S. & Pienkos, P. T. Proteomic analysis of Chlorella vulgaris: potential targets for enhanced lipid accumulation. *J Proteomics* **93**, 245-253, doi:10.1016/j.jprot.2013.05.025 (2013).
10 Minhas, A. K., Hodgson, P., Barrow, C. J. & Adholeya, A. A Review on the Assessment of Stress Conditions for Simultaneous Production of Microalgal Lipids and Carotenoids. *Front Microbiol* **7**, 546, doi:10.3389/fmicb.2016.00546 (2016).
11 Martin, S. F., Munagapati, V. S., Salvo-Chirnside, E., Kerr, L. E. & Le Bihan, T. Proteome turnover in the green alga Ostreococcus tauri by time course 15N metabolic labeling mass spectrometry. *J Proteome Res* **11**, 476-486, doi:10.1021/pr2009302 (2012).
12 Lohman, E. J. *et al.* Optimized inorganic carbon regime for enhanced growth and lipid accumulation in Chlorella vulgaris. *Biotechnol Biofuels* **8**, 82, doi:10.1186/s13068-015-0265-4 (2015).
13 Levering, J., Dupont, C. L., Allen, A. E., Palsson, B. O. & Zengler, K. Integrated Regulatory and Metabolic Networks of the Marine Diatom Phaeodactylum tricornutum Predict the Response to Rising CO2 Levels. *mSystems* **2**, doi:10.1128/mSystems.00142-16 (2017).
14 Chen, Y., Xu, C. & Vaidyanathan, S. Microalgae: a robust "green bio-bridge" between energy and environment. *Crit Rev Biotechnol*, 1-18, doi:10.1080/07388551.2017.1355774 (2017).
15 O'Neill, J. S. *et al.* Circadian rhythms persist without transcription in a eukaryote. *Nature* **469**, 554-558, doi:10.1038/nature09654 (2011).

16 Leliaert, F., Verbruggen, H. & Zechman, F. W. Into the deep: new discoveries at the base of the green plant phylogeny. *Bioessays* **33**, 683-692, doi:10.1002/bies.201100035 (2011).
17 Courties, C. *et al.* Phylogenetic analysis and genome size of Ostreococcus tauri (Chlorophyta, Prasinophyceae). *J Phycol* **34**, 844-849, doi:DOI 10.1046/j.1529-8817.1998.340844.x (1998).
18 Guillou, L. *et al.* Diversity of picoplanktonic prasinophytes assessed by direct nuclear SSU rDNA sequencing of environmental samples and novel isolates retrieved from oceanic and coastal marine ecosystems. *Protist* **155**, 193-214, doi:10.1078/143446104774199592 (2004).
19 Cardol, P. *et al.* An original adaptation of photosynthesis in the marine green alga Ostreococcus. *Proc Natl Acad Sci U S A* **105**, 7881-7886, doi:10.1073/pnas.0802762105 (2008).
20 Derelle, E. *et al.* Genome analysis of the smallest free-living eukaryote Ostreococcus tauri unveils many unique features. *Proc Natl Acad Sci U S A* **103**, 11647-11652, doi:10.1073/pnas.0604795103 (2006).
21 Blanc-Mathieu, R. *et al.* Population genomics of picophytoplankton unveils novel chromosome hypervariability. *Sci Adv* **3**, e1700239, doi:10.1126/sciadv.1700239 (2017).
22 Smallwood, C. R. *et al.* Ostreococcus tauri is a high-lipid content green algae that extrudes clustered lipid droplets. *bioRxiv*, doi:10.1101/249052 (2018).
23 Le Bihan, T. *et al.* Label-free quantitative analysis of the casein kinase 2-responsive phosphoproteome of the marine minimal model species Ostreococcus tauri. *Proteomics* **15**, 4135-4144, doi:10.1002/pmic.201500086 (2015).
24 McCoy, J. G. *et al.* Discovery of sarcosine dimethylglycine methyltransferase from Galdieria sulphuraria. *Proteins* **74**, 368-377, doi:10.1002/prot.22147 (2009).
25 Luo, G. Z., Blanco, M. A., Greer, E. L., He, C. & Shi, Y. DNA N(6)-methyladenine: a new epigenetic mark in eukaryotes? *Nat Rev Mol Cell Biol* **16**, 705-710, doi:10.1038/nrm4076 (2015).
26 Degraeve-Guilbault, C. *et al.* Glycerolipid Characterization and Nutrient Deprivation-Associated Changes in the Green Picoalga Ostreococcus tauri. *Plant Physiol* **173**, 2060-2080, doi:10.1104/pp.16.01467 (2017).
27 Shimojima, M. & Ohta, H. Critical regulation of galactolipid synthesis controls membrane differentiation and remodeling in distinct plant organs and following environmental changes. *Prog Lipid Res* **50**, 258-266, doi:10.1016/j.plipres.2011.03.001 (2011).
28 Schaller-Laudel, S. *et al.* Influence of thylakoid membrane lipids on the structure of aggregated light-harvesting complexes of the diatom Thalassiosira pseudonana and the green alga Mantoniella squamata. *Physiol Plant* **160**, 339-358, doi:10.1111/ppl.12565 (2017).
29 Losh, J. L., Young, J. N. & Morel, F. M. Rubisco is a small fraction of total protein in marine phytoplankton. *The New phytologist* **198**, 52-58, doi:10.1111/nph.12143 (2013).
30 Noordally, Z. B. *et al.* Circadian protein regulation in the green lineage I. A phospho-dawn anticipates light onset before proteins peak in daytime. *bioRxiv*, doi:10.1101/287862 (2018).

31 Keller, M. D., Selvin, R. C., Claus, W. & Guillard, R. R. L. Media for the Culture of Oceanic Ultraphytoplankton. *J Phycol* **23**, 633-638 (1987).
32 Ji, Y. *et al.* Raman spectroscopy provides a rapid, non-invasive method for quantitation of starch in live, unicellular microalgae. *Biotechnol J* **9**, 1512-1518, doi:10.1002/biot.201400165 (2014).
33 Le Gros, M. A. *et al.* Biological soft X-ray tomography on beamline 2.1 at the Advanced Light Source. *J Synchrotron Radiat* **21**, 1370-1377, doi:10.1107/S1600577514015033 (2014).
34 Parkinson, D. Y., Knoechel, C., Yang, C., Larabell, C. A. & Le Gros, M. A. Automatic alignment and reconstruction of images for soft X-ray tomography. *J Struct Biol* **177**, 259-266, doi:10.1016/j.jsb.2011.11.027 (2012).
35 Dautel, S. E. *et al.* Lipidomics reveals dramatic lipid compositional changes in the maturing postnatal lung. *Sci Rep* **7**, 40555, doi:10.1038/srep40555 (2017).
36 Kyle, J. E. *et al.* LIQUID: an-open source software for identifying lipids in LC-MS/MS-based lipidomics data. *Bioinformatics* **33**, 1744-1746, doi:10.1093/bioinformatics/btx046 (2017).
37 Wang, Y. *et al.* Reversed-phase chromatography with multiple fraction concatenation strategy for proteome profiling of human MCF10A cells. *Proteomics* **11**, 2019-2026, doi:10.1002/pmic.201000722 (2011).
38 Eng, J. K., McCormack, A. L. & Yates, J. R. An approach to correlate tandem mass spectral data of peptides with amino acid sequences in a protein database. *J Am Soc Mass Spectrom* **5**, 976-989, doi:10.1016/1044-0305(94)80016-2 (1994).
39 Kim, S., Gupta, N. & Pevzner, P. A. Spectral probabilities and generating functions of tandem mass spectra: a strike against decoy databases. *J Proteome Res* **7**, 3354-3363, doi:10.1021/pr8001244 (2008).
40 Monroe, M. E., Shaw, J. L., Daly, D. S., Adkins, J. N. & Smith, R. D. MASIC: a software program for fast quantitation and flexible visualization of chromatographic profiles from detected LC-MS(/MS) features. *Comput Biol Chem* **32**, 215-217, doi:10.1016/j.compbiolchem.2008.02.006 (2008).

Main Figures

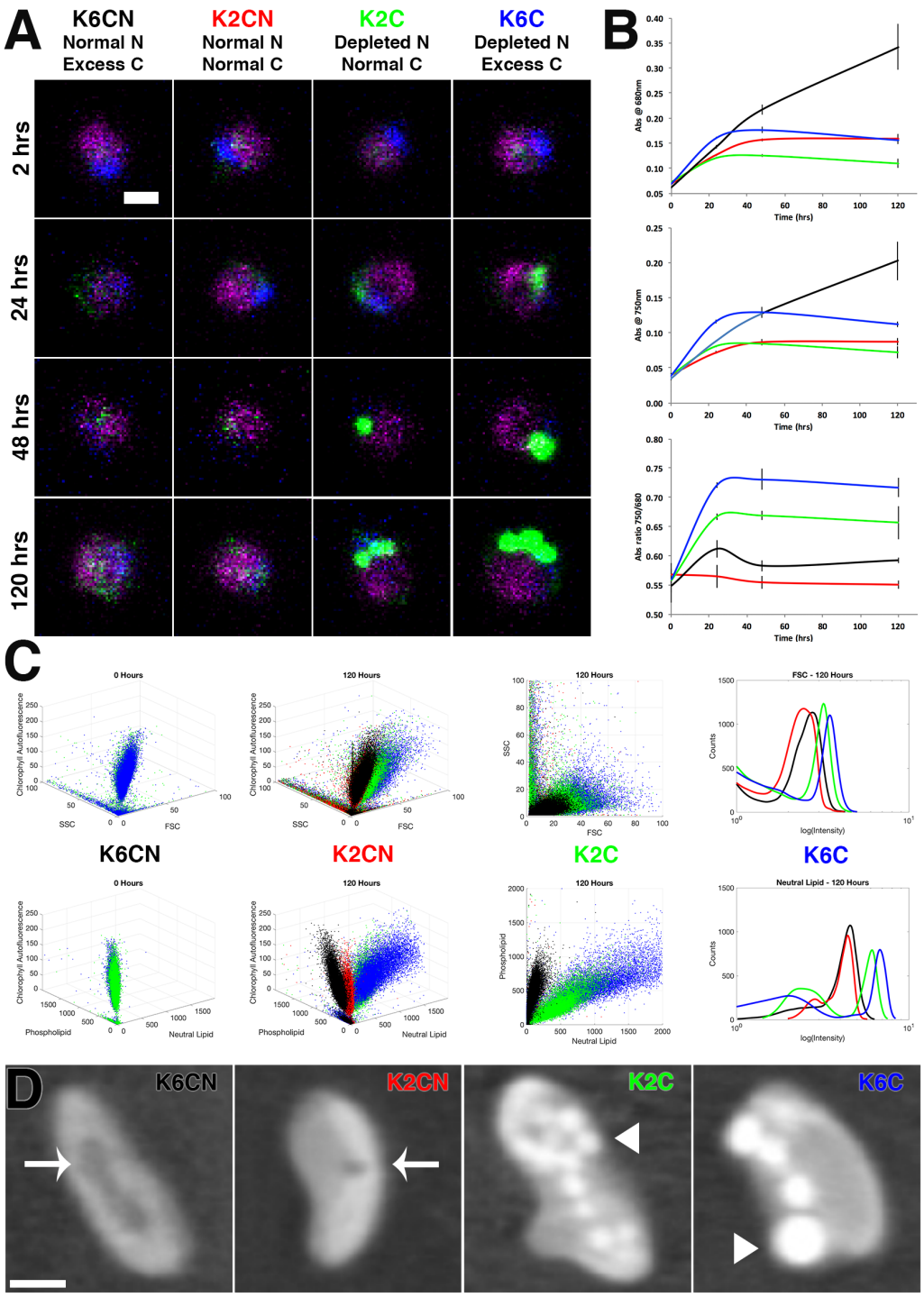

Figure 1 Single cell and population imaging and growth under varying C:N ratios
(A) Confocal microscopy of K6CN, K2CN, K2C, and K6C cultures to observe chlorophyll autofluorescence (magenta), nucleic acid fluorescent staining (blue), neutral lipid fluorescent staining (green) over time. Scale bar represents 1µm scale. (B) Corresponding growth plots for the same cultures monitored over time (error bars represent a replicate of 5) at 750nm and 680nm, and the ratio of the 750/680 as a measure of photosynthetic efficiency. (C) FACS time course study of same cultures comparing SSC (side-scattering) versus FSC (forward scattering) and chlorophyll autofluorescence in 3D plots at 0 hours and 120 hours, then 2D plot of SSC versus FSC at 120 hours, and histogram of FSC at 120 hours. (D) FACS time course study of same

cultures comparing phospholipid versus neutral lipid and chlorophyll autofluorescence in 3D plots at 0 hours and 120 hours, then 2D plot of phospholipid versus neutral lipid at 120 hours, and histogram of neutral lipid at 120 hours. (E) Label-free cryogenic soft x-ray nanotomography images of cells cryogenically frozen in microcapillaries. Central slices (1µm scale bar) display intracellular structures common to each culture condition. Chloroplasts and cytoplasm seen in all images. Vacuoles in K6CN and K2CN appear as dark objects indicated with white arrow. Lipid droplets appear as bright white circular objects indicated by white arrowhead.

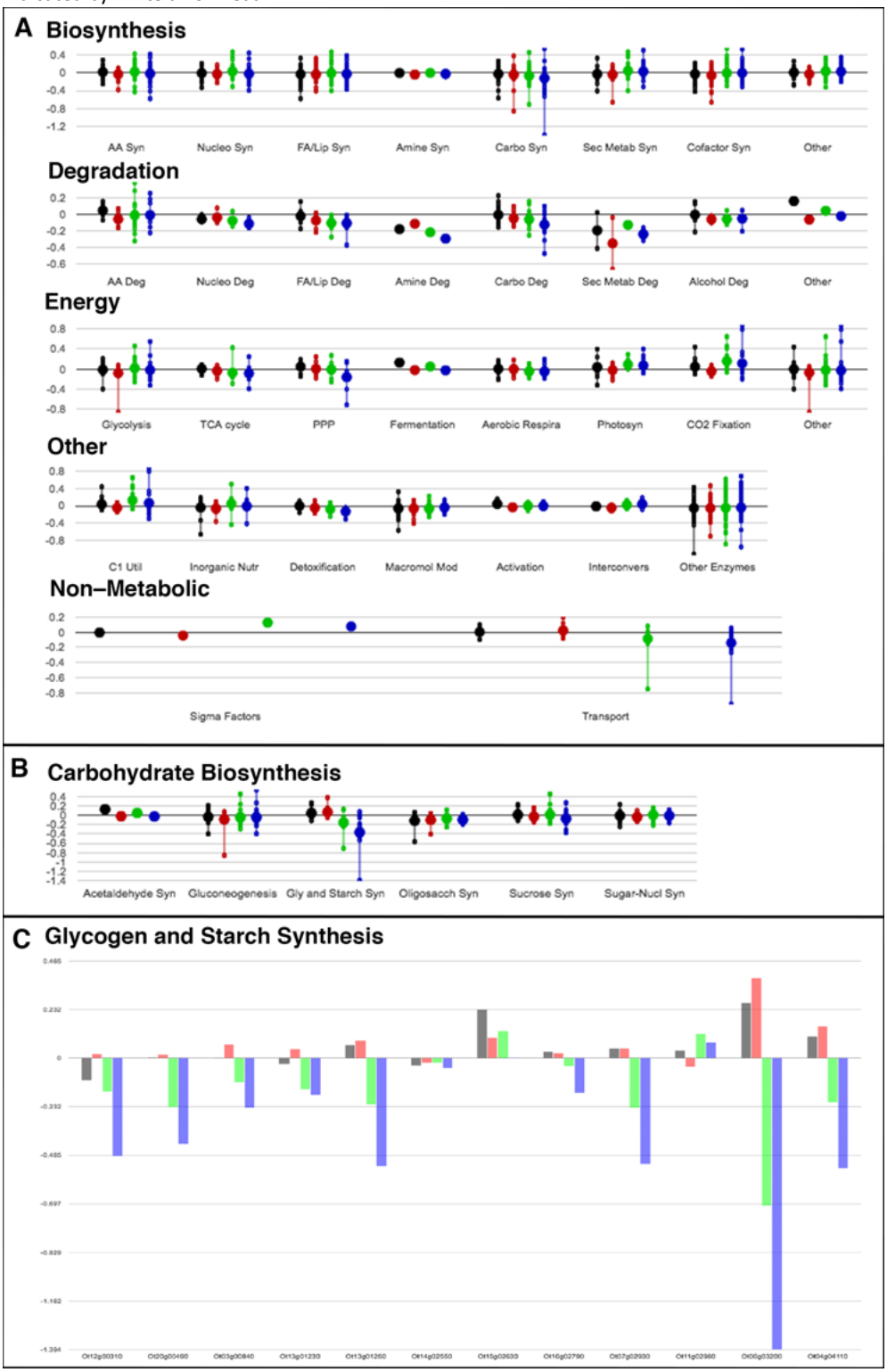

Figure 2 Metabolic pathway mapping of global proteomics
O. tauri cells cultured in K6CN (black), K2CN (red), K2C (green), K6C (blue) at 48 hours relative to cultures from K2CN at 24 hours were grouped and mapped by metabolic pathway(A), subpathway (B), and individual proteins (C). Each large circle represents an average level of abundance on a log2 scale where negative values are increases in abundance relative to cell conditions K2CN at 24 hours. Smaller circles represent individual proteins in the respective metabolic pathway.

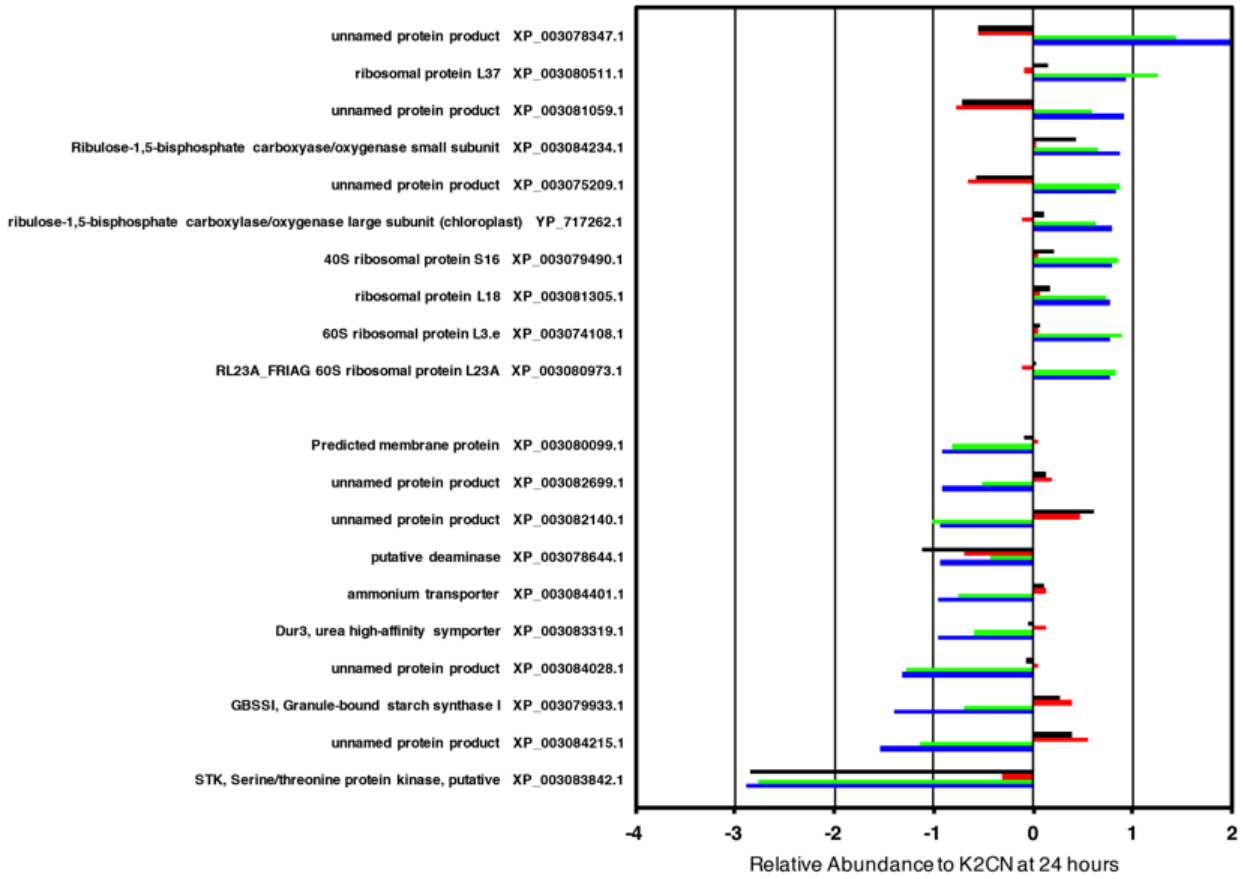

Figure 3 Selection differentially expressed proteins from global proteomics of varying N and C conditions
Abundance profiles for 10 most downregulated (positive values) and upregulated (negative values) proteins comparing K2CN at 24 hours versus K6CN at 48 hours (black), K2CN at 48 hours (red), K2C at 48 hours (green), and K6C at 48 hours (blue) cell cultures.

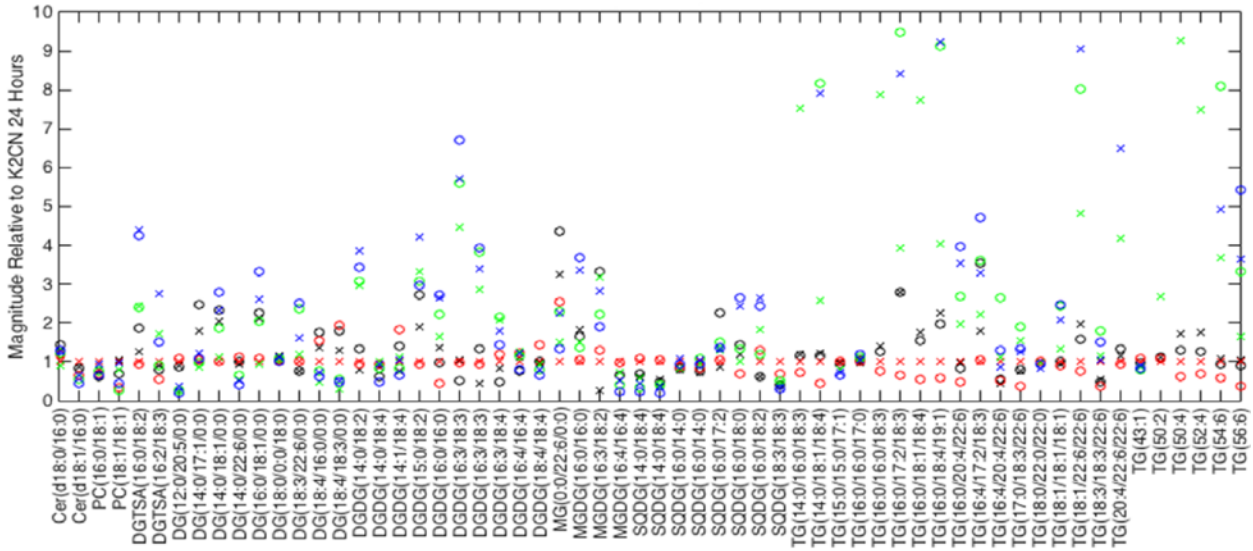

Figure 4 Time resolved differential expression of global lipids

Selection of lipids (out of 287) detected via LC-MS/MS for cell cultures at 24 (X symbols) and 48 hours (O symbols) for varying C:N ratio conditions K6CN (black), K2CN (red), K2C (green) and K6C (blue). *Cer: Ceramide; PC: phosphatidylcholine; MGDG: monogalactosyldiacylglycerol; DG: diacylglycerol; DGDG: digalactosyldiacylglycerol; DGTSA: diacylglyceryl trimethylhomoserine or diacylglyceryl trimethyl-beta-alanine; SQDG: sulfoquinovosyldiacylglycerol; and TG: triacylglycerols*

Supplemental Figures

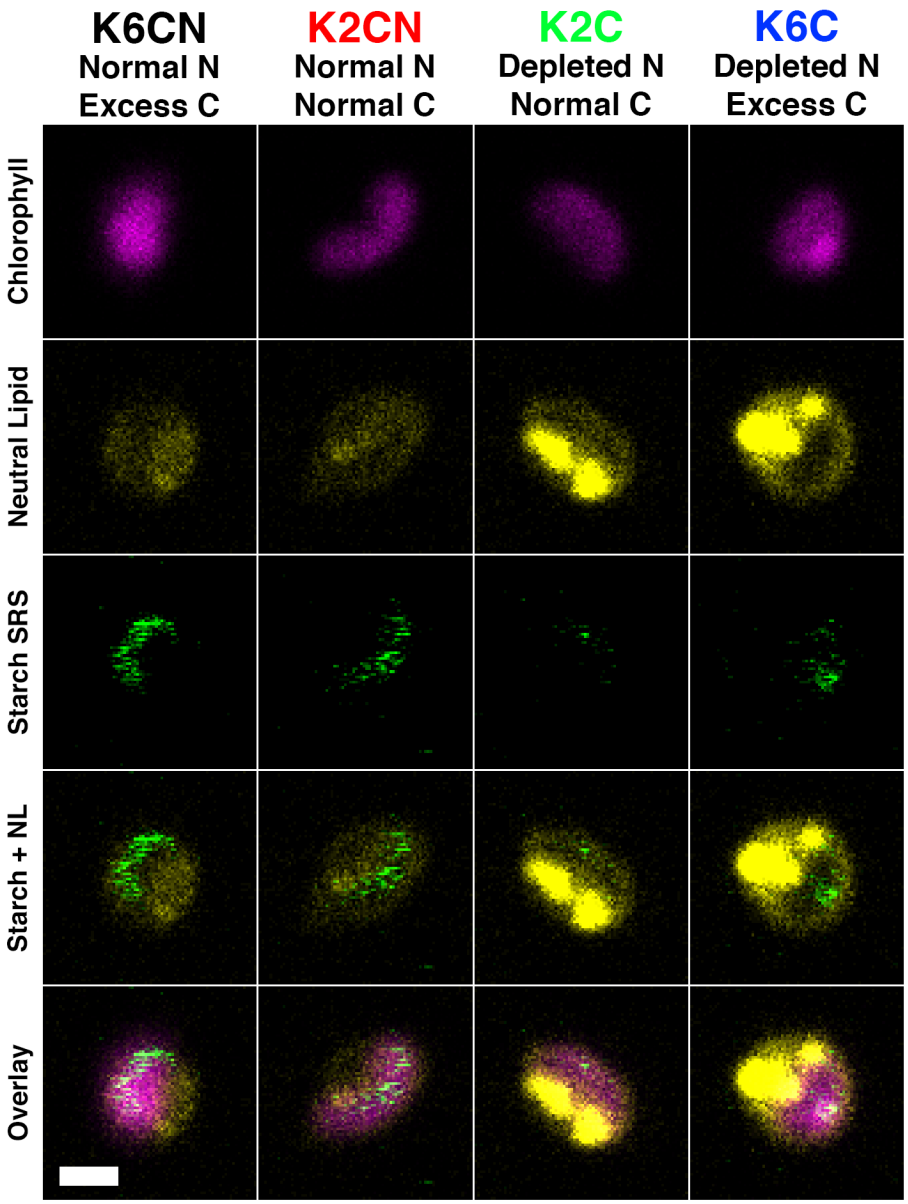

Supplemental Figure 1 Fluorescence and SRS verification of neutral lipid and starch accumulation
Fluorescence and SRS microscopy were conducted on *O. tauri* cells stained with Nile Red from various C:N conditions after 96 hours of starvation. Chlorophyll autofluorescence (pink) was observed in all cells with neutral lipid (yellow) and SRS starch signal (green). Elevated neutral lipid was observed in K2C and K6C cells localized outside the chloroplast. Starch was detected and localized to the chloroplast for K6CN, K2CN, and to a lesser extent K6C, with little to no starch signal found in K2C cells. Scale bar represents 1µm.

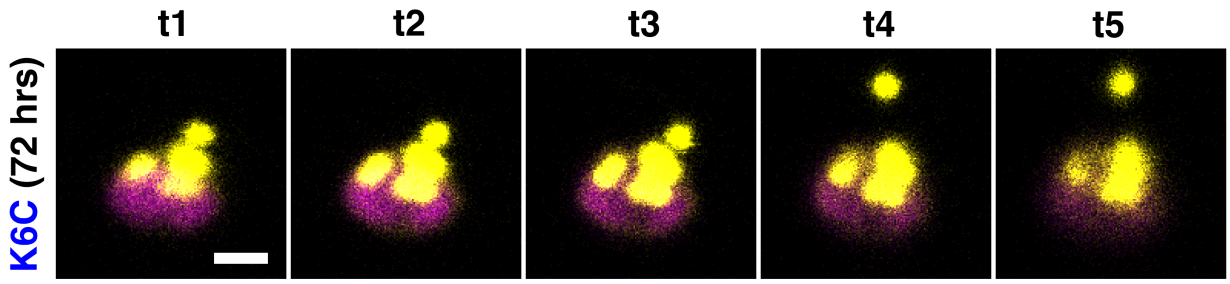

Supplemental Figure 2 Time course of lipid release from cells into intercellular space
O. tauri cells cultured in K6C media for 72 hours were harvested and stained with Nile Red and then imaged by confocal fluorescence microscopy. Chlorophyll autofluorescence (pink) and neutral lipid (yellow) revealed many large lipid bodies during z-slice imaging and a single lipid body release was tracked over time (t) in intercellular milieu while other lipids remained inside the intracellular space.

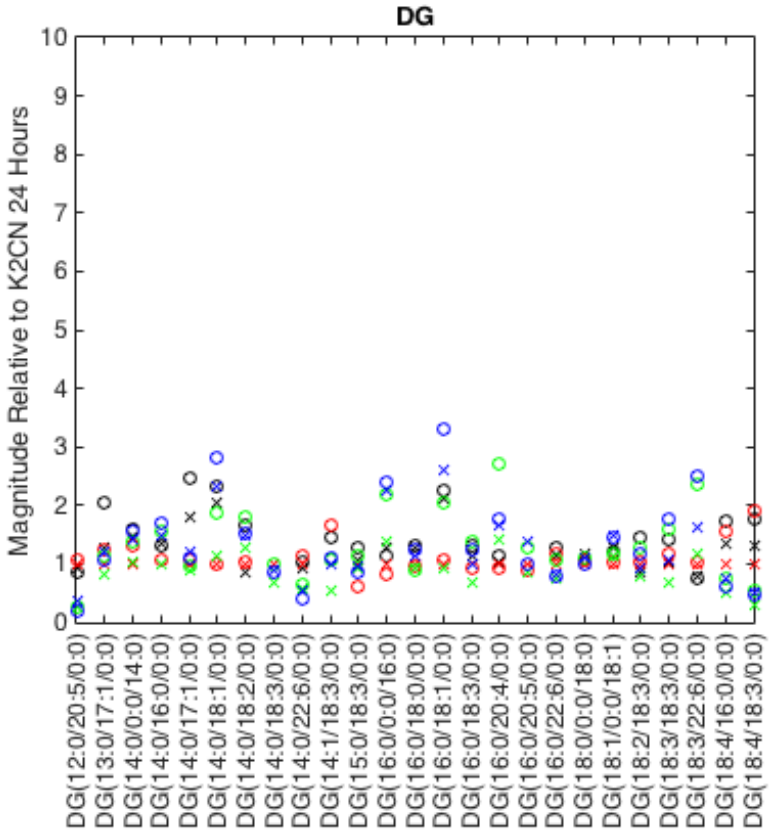

Supplemental Figure 3 Time-resolved lipidomics of diacylglycerol lipids
Diacylglycerol (DG) lipids detected via LC-MS/MS for cell cultures at 24 (X symbols) and 48 hours (O symbols) for varying C:N ratio conditions K6CN (black), K2CN (red), K2C (green) and K6C (blue) relative to K2CN at 24 hours (y-axis).

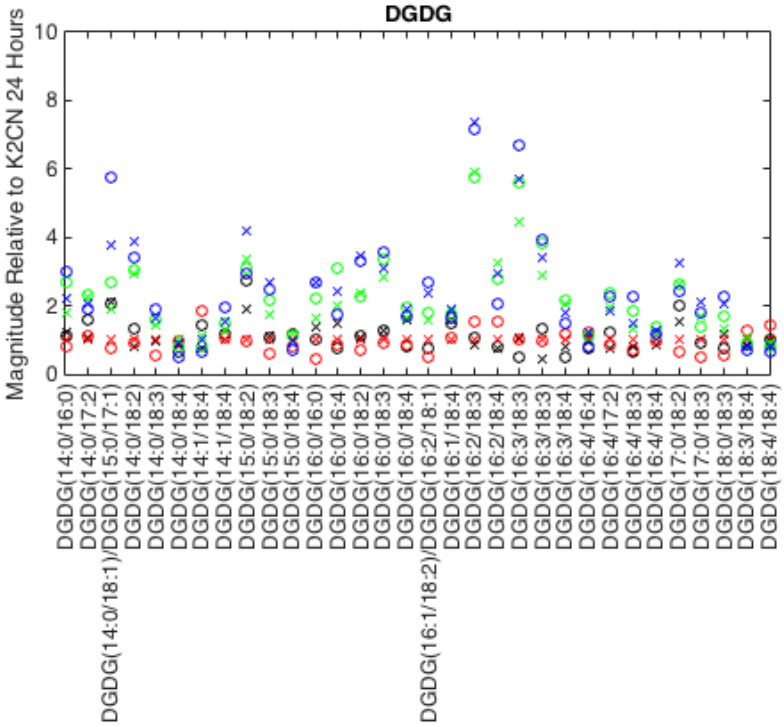

Supplemental Figure 4 Time resolved differential expression of digalactosyldiacylglycerol lipids
Digalactosyldiacylglycerol (DGDG) lipids detected for cell cultures at 24 (X symbols) and 48 hours (O symbols) for varying C:N ratio conditions K6CN (black), K2CN (red), K2C (green) and K6C (blue) relative to K2CN at 24 hours (y-axis).

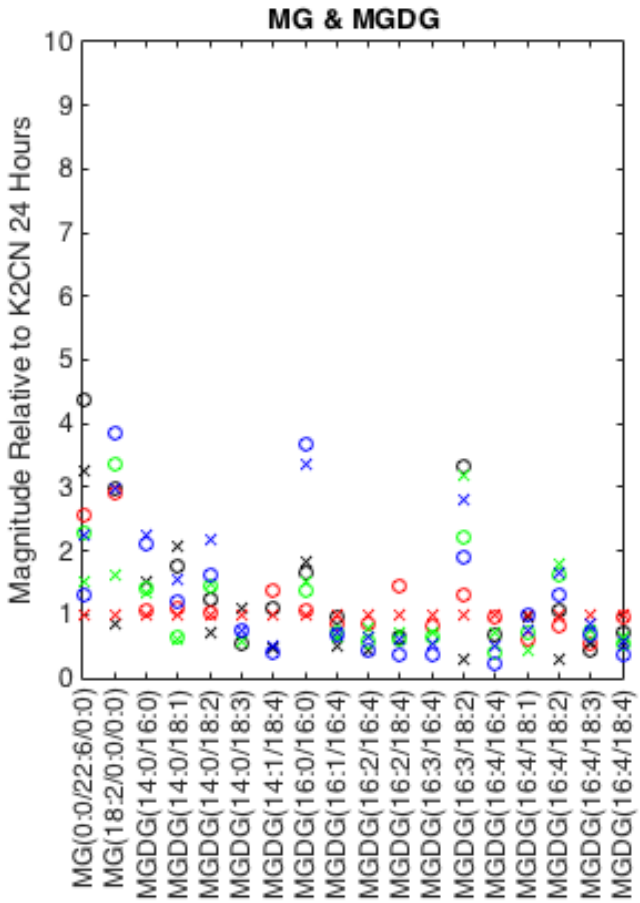

Supplemental Figure 5 Time resolved differential expression of monoacylglycerol and monogalactosyldiacylglycerol lipids
Monoacylglycerol (MG) and monogalactosyldiacylglycerol (MGDG) lipids detected via LC-MS/MS for cell cultures at 24 (X symbols) and 48 hours (O symbols) for varying C:N ratio conditions K6CN (black), K2CN (red), K2C (green) and K6C (blue) relative to K2CN at 24 hours (y-axis).

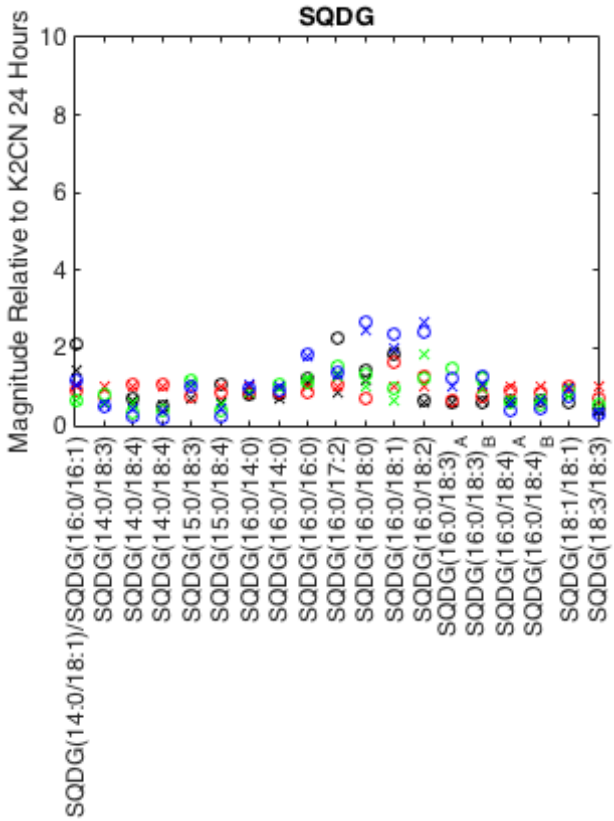

Supplemental Figure 6 Time resolved differential expression of lipids
Sulfoquinovosyldiacylglycerol (SQDG) lipids detected via LC-MS/MS for cell cultures at 24 (X symbols) and 48 hours (O symbols) for varying C:N ratio conditions K6CN (black), K2CN (red), K2C (green) and K6C (blue) relative to K2CN at 24 hours (y-axis).

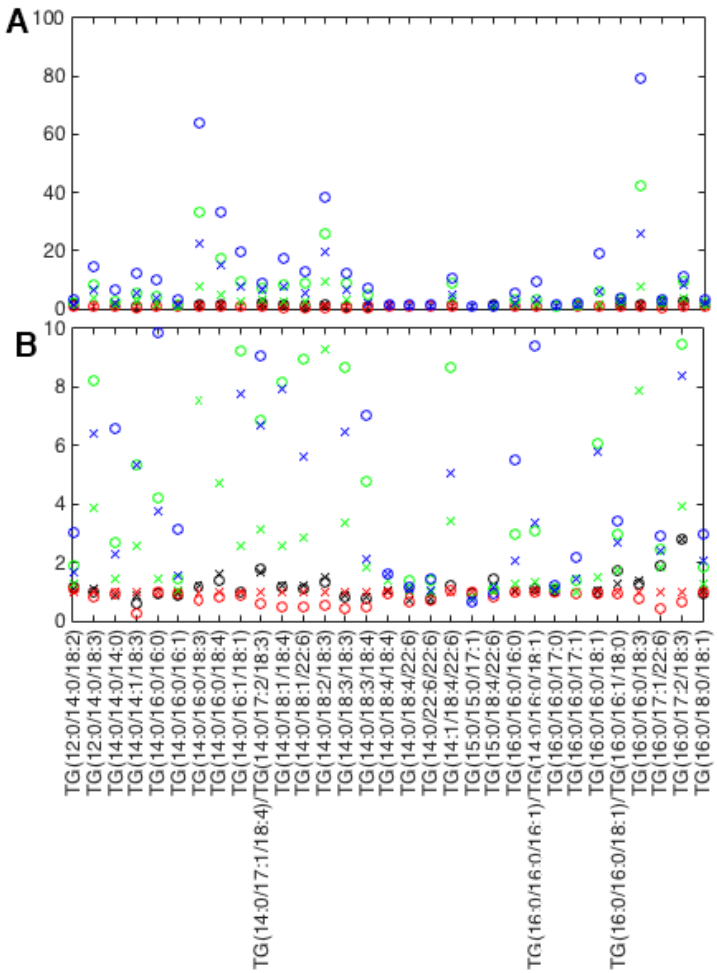

Supplemental Figure 7 Time resolved differential abundance of triacylglycerol lipids set 1
Triacylglycerol (TG) lipidomics for cell cultures at 24 (X symbols) and 48 hours (O symbols) for varying C:N ratio conditions K6CN (black), K2CN (red), K2C (green) and K6C (blue) relative to K2CN at 24 hours (y-axis).

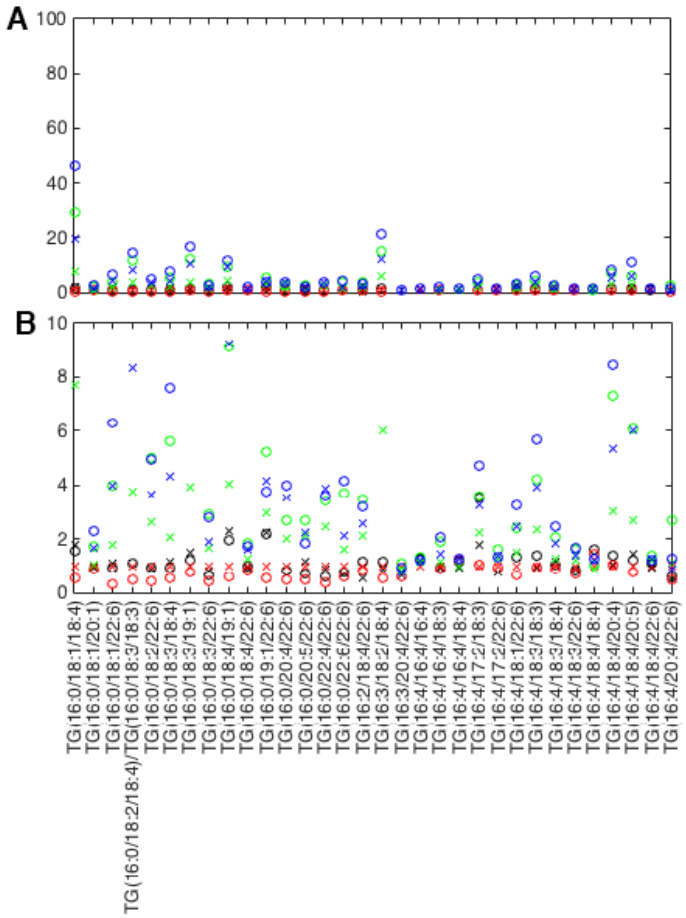

Supplemental Figure 8 Time resolved differential abundance of triacylglycerol lipids, set 2
Triacylglycerol (TG) lipidomics detected via LC-MS/MS for cell cultures at 24 (X symbols) and 48 hours (O symbols) for varying C:N ratio conditions K6CN (black), K2CN (red), K2C (green) and K6C (blue) relative to K2CN at 24 hours (y-axis).

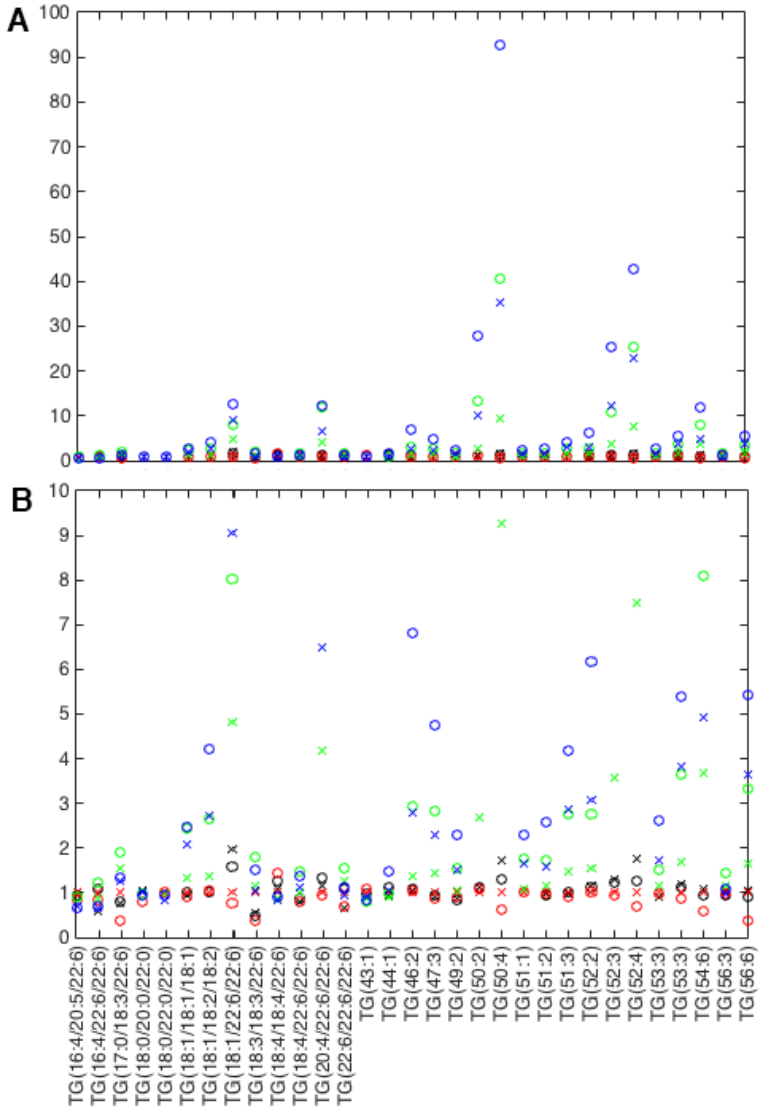

Supplemental Figure 9 Time resolved differential abundance of long chain triacylglycerol lipids, scale 10
Long chain triacylglycerol (TG) lipidomics for cell cultures at 24 (X symbols) and 48 hours (O symbols) for varying C:N ratio conditions K6CN (black), K2CN (red), K2C (green) and K6C (blue) relative to K2CN at 24 hours (y-axis).